Zernike analysis of all-sky night brightness maps

Salvador Bará,[1,*] Miguel Nievas,[2] Alejandro Sánchez de Miguel,[3] and Jaime Zamorano[3]

[1]Área de Óptica, Dept. de Física Aplicada, Fac. de Física, Universidade de Santiago de Compostela, 15782 Santiago de Compostela, Galicia, Spain

[2]Dept. de Física Atómica, Molecular y Nuclear, Fac. de Ciencias Físicas, Universidad Complutense, Madrid, Spain

[3]Dept. de Astrofísica y CC. de la Atmósfera, Fac. de Ciencias Físicas, Universidad Complutense, Madrid, Spain

*Corresponding author: salva.bara@usc.es

Received 23 January 2014; revised 20 March 2014; accepted 21 March 2014;
posted 21 March 2014 (Doc. ID 205177); published 17 April 2014

All-sky night brightness maps (calibrated images of the night sky with hemispherical field-of-view (FOV) taken at standard photometric bands) provide useful data to assess the light pollution levels at any ground site. We show that these maps can be efficiently described and analyzed using Zernike circle polynomials. The relevant image information can be compressed into a low-dimensional coefficients vector, giving an analytical expression for the sky brightness and alleviating the effects of noise. Moreover, the Zernike expansions allow us to quantify in a straightforward way the average and zenithal sky brightness and its variation across the FOV, providing a convenient framework to study the time course of these magnitudes. We apply this framework to analyze the results of a one-year campaign of night sky brightness measurements made at the UCM observatory in Madrid. © 2014 Optical Society of America

OCIS codes: (010.1290) Atmospheric optics; (110.0110) Imaging systems; (100.2960) Image analysis.
http://dx.doi.org/10.1364/AO.53.002677

1. Introduction

Light pollution, i.e., the alteration of the natural levels of night darkness due to the artificial emissions of light, is an emerging issue that in the last years aroused considerable interest among the scientific community. A growing body of research has revealed the potentially detrimental effects of the inadequate use of light-at-night on science, ecology, physiology, energy consumption, and intangible heritage [1–6]. Modeling the light pollution propagation through the atmosphere is an active field of research [7–12] with direct practical applications for the correct design of urban lighting systems.

One of the most conspicuous manifestations of light pollution is increased sky glow [1]. The scattering of artificial light in the atmosphere increases the brightness of the night sky background creating a veil that jeopardizes contrast and hinders ground-based observations of celestial bodies. A way of monitoring this effect is by means of all-sky (hemispherical) images of the night sky taken in standard photometric bands [13–16]. In contrast with their rather coarse spectral resolution, the spatial resolution of all-sky images is relatively high, due to the big number of pixels available in present day scientific grade CCD detectors. The brightness distribution recorded in these images has several components: besides the slowly variant contribution due to the scattering of artificial light, they generally contain the images of point-like natural sources (stars and planets), urban or natural obstacles such as buildings or trees, and possibly artificial lights near the horizon. They are affected by several sources of random noise, dependent on the incoming photon flux, the photometric band, and the detector performance.

The relatively smooth spatial distribution of the artificial light scattered by the atmosphere across the hemispherical field-of-view (FOV) suggests that it can be efficiently described in terms of a suitable polynomial basis.

1559-128X/14/122677-10$15.00/0

One of those bases is formed by the well-known Zernike circle polynomials, whose applications in optics and astronomy have been thoroughly explored since their introduction by Zernike in the first-half of the XX century [17–21]. The main purpose of this work is to show the advantages of using Zernike polynomial series to analyze the measured all-sky night brightness distributions. We show, on the one hand, that the relevant information contained in all-sky images can be compressed into a small set of coefficients with definite physical meaning. From these coefficients several useful parameters, as, e.g., the average and zenithal sky brightness, its variation across the FOV, and its time course throughout the night can be easily determined. On the other hand, fitting a low to medium order Zernike series is an effective way of filtering out the effects of noise and removing the isolated point-like sources that may be present within the FOV. These high spatial frequency image components manifest themselves as the residuals of the polynomial fit. Additionally, since the Zernike representation provides sky brightness information that is defined over the whole hemisphere and is independent from the particular sampling grid used to acquire the brightness raw data, it can be expected that this approach will facilitate the intercomparison of results among all-sky cameras installed around the world to monitor light pollution.

The structure of the paper is as follows: in Section 2 we briefly outline the basic properties of the Zernike polynomials and describe the estimation approach used to fit the Zernike expansion to the all-sky night brightness images. Section 3 describes the results of the analysis of a set of cloudless and moonless night brightness maps acquired during one year of observations at the astronomical observatory of the Universidad Complutense in Madrid. Additional remarks and conclusions are drawn in Sections 4 and 5, respectively.

2. Zernike Expansion of All-Sky Night Brightness Maps

A. All-Sky Night Brightness Maps

An all-sky night brightness map is a calibrated image of the celestial vault taken at a standard photometric band (Fig. 1). Its FOV spans the complete upper hemisphere, from zenith to horizon, mapped onto a plane surface according to a suitable projection scheme. Mappings that preserve the element of area are particularly adequate for the modal analysis of all-sky images. In this kind of projection, equally sized regions of the map correspond to equal solid angles in the sky, and therefore one can integrate over solid angles across the FOV by integrating over the corresponding regions of the flat map. This property, in combination with the orthonormality of the Zernike polynomials over the unit-radius circle, allows one to ascribe a definite physical meaning to the Zernike modal coefficients, as we will show below. One example of such area-preserving mappings is the Lambert's azimuthal equal-area projection [22] used in Fig. 1.

Since the Zernike polynomials are orthonormal in the unit-radius circle, we will henceforth describe the position of any point of the image in terms of its normalized coordinates $\mathbf{r} = (x, y)$, where $x = X/R$ and $y = Y/R$, being (X, Y) the absolute cartesian coordinates measured from the zenith and R the radius of the circle delimited by the horizon line. The value of the all-sky image at point $\mathbf{r}$ will be denoted by $S(\mathbf{r})$.

Although raw all-sky images are useful to get qualitative information of the night sky brightness across the celestial vault, they have to be calibrated in order to obtain all-sky maps of radiances. The calibration procedure includes correcting for the spatial and spectral responses of the camera. The spatial response of the system across the FOV is determined with optical laboratory tests. After the observations, the images were corrected for distortion. From the geographical position of the camera, and the date and time of the observation, the expected positions of the stars on the image were derived and compared with the recorded ones, obtaining the appropriate transformation equations. The images were subsequently processed following the standard procedures used for CCD astronomical observations with the help of calibration frames. The original 16 bit RAW images were corrected for bias and thermal noise using a master dark frame, and for the spatial sensitivity variation with a master flat frame for each photometric filter. In the second step, the photometric calibration was performed by comparing the magnitudes of standard stars with the measured fluxes, which provides the instrumental zero point. Finally the pixel values were converted from ADUs per second per pixel to radiance units using the zero point, the spatial scale of the image (in

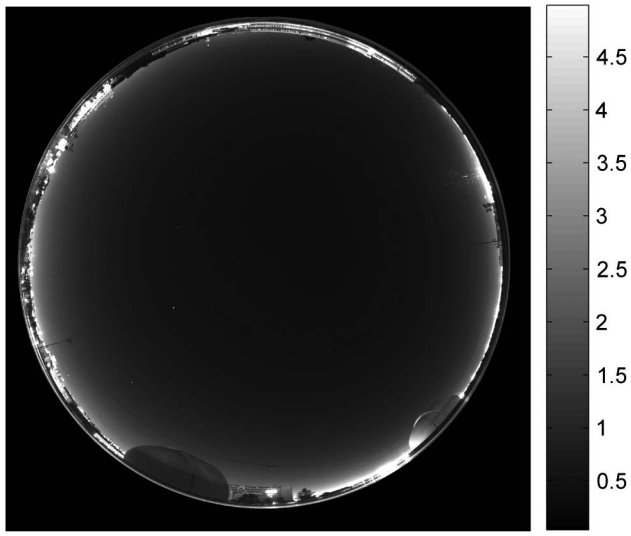

Fig. 1. All-sky night brightness map taken in the Johnson–Cousin's V-band at the astronomical observatory of Universidad Complutense, Madrid, in December 8, 2012, at 21:28 (UT) using an ASTMON camera. The observatory domes can be seen at the lower rim of the image. Gray scale in units mJy/arcsec^2.

arcsec^2/pixel), and the conversion factor from magnitudes to radiances for each photometric band [23].

Pixel values represent the spectral radiance averaged within the passband of the corresponding photometric filter. Sky spectral radiances are often expressed in Jansky per square arcsecond (Jy/arcsec^2), instead of the conventional SI units W/(m$^2\cdot$Hz$\cdot$sr) or W/(m$^2\cdot$nm$\cdot$sr). The conversion between both unit systems is immediate, taking into account that $1\ \text{Jy} = 10^{-26}\ \text{W/(m}^2\cdot\text{Hz)}$ and $1\ \text{arcsec}^2 = 2.35\times10^{-11}$ sr.

B. Zernike Polynomial Basis

The Zernike circle polynomials are an orthonormal basis set of functions whose general form in polar coordinates $\mathbf{r} = (r,\theta)$ is given by [17–21]

$$Z_{n,m}(\mathbf{r}) = N_{n,m}R_{n,m}(r)A_m(\theta), \tag{1}$$

where n and m are the radial and angular orders, respectively, of the $Z_{n,m}$ mode, $R_{n,m}(r)$ is its radial part given by

$$R_{n,m}(r) = \sum_{l=0}^{(n-|m|)/2} \frac{(-1)^l(n-l)!}{l![0.5(n+|m|)-l]![0.5(n-|m|)-l]!}r^{n-2l} \tag{2}$$

whose value at the rim is $R_{n,m}(1) = 1$, and $A_m(\theta)$ is the angular part defined as

$$A_m(\theta) = \begin{cases} \cos m\theta, & \text{for } m \geq 0 \\ \sin |m|\theta, & \text{for } m < 0 \end{cases} \tag{3}$$

with $m = -n, -n+2, \ldots, n-2, n$. Zernike modes with $m = 0$ are azimuthally symmetric; the remaining ones have m-fold rotational symmetry. The normalization constant $N_{n,m}$ is usually chosen as

$$N_{n,m} = \sqrt{(2-\delta_{m0})(n+1)}, \tag{4}$$

where δ_{m0} is the Kronecker delta ($\delta_{pq} = 1$ if and only if $p = q$; otherwise $\delta_{pq} = 0$). With this choice, the Zernike polynomials are orthonormal in the unit radius circle according to

$$\frac{1}{\pi}\int_{r=0}^{1}\int_{\theta=0}^{2\pi} Z_{n,m}(\mathbf{r})Z_{n',m'}(\mathbf{r})r\mathrm{d}r\mathrm{d}\theta = \delta_{nn'}\delta_{mm'}. \tag{5}$$

For notational convenience, the double-index ordering $Z_{n,m}(\mathbf{r})$ can be transformed into a single-index one, $Z_k(\mathbf{r})$, with

$$k = [n(n+2)+m]/2 + 1. \tag{6}$$

This definition of k differs in one unit from that of the single-index j that can be found in [21]. This change is made here in order to assign to the first Zernike mode (the constant term or piston, $n = m = 0$) the index $k = 1$ instead of 0. This choice allows for an easier indexing of the elements of the matrices that will be defined below. Excepting for the first mode (piston), which is constant, $Z_1(\mathbf{r}) \equiv Z_{0,0}(\mathbf{r}) = 1$, the average value of any Zernike mode within its circular definition domain is zero. This can be immediately deduced from the orthonormality condition in Eq. (5) by setting $n' = m' = 0$.

Figure 2 shows the shapes of several Zernike modes of different radial and angular orders. Surface plots for other modes can be found in [19].

Since the Zernike polynomials are a complete set of functions, the actual night sky brightness, $B(\mathbf{r})$, can be expanded in terms of an *a priori* infinite series as

$$B(\mathbf{r}) = \sum_{n=0}^{\infty}\sum_{m=-n}^{n} a_{n,m}Z_{n,m}(\mathbf{r}) \equiv \sum_{k=1}^{\infty} a_k Z_k(\mathbf{r}), \tag{7}$$

where the $a_k (k = 1, \ldots, \infty)$, in spectral radiance units, are the actual (as opposed to estimated) Zernike coefficients of the map. These modal coefficients are the analytical projections of $B(\mathbf{r})$ over the corresponding element of the basis, such that

$$a_k = \frac{1}{\pi}\int_{r=0}^{1}\int_{\theta=0}^{2\pi} B(\mathbf{r})Z_k(\mathbf{r})r\mathrm{d}r\mathrm{d}\theta, \tag{8}$$

as it can be straightforwardly deduced by substituting Eq. (7) for $B(\mathbf{r})$ into Eq. (8) and making use of the orthonormality relations in Eq. (5).

In practice the series in Eq. (7) is truncated at a finite radial order $n = n_{\max}$, which is sufficiently high as to ensure that the differences between the exact and the truncated series are negligible. On the other hand, the integration in Eq. (8) cannot be analytically performed in the continuum of the unit radius circle because the experimental data are always discrete all-sky images $S(\mathbf{r})$ with a finite number of pixels. Furthermore, the experimental all-sky

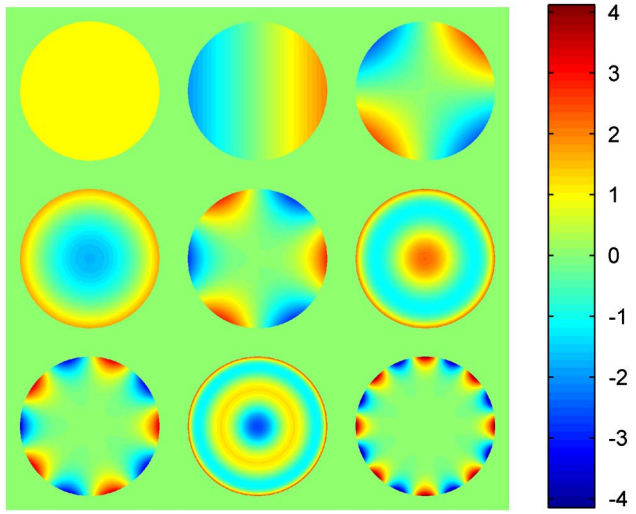

Fig. 2. From left to right and top to bottom: Plots of the Zernike modes of indices $k(n,m)$: 1 (0,0); 3(1,+1); 4 (2,–2); 5 (2,0); 10 (3,+3); 13 (4,0); 21 (5,+5); 25 (6,0); and 45 (8,+8).

brightness maps are noise-degraded versions of the actual $B(\mathbf{r})$, such that

$$S(\mathbf{r}) = B(\mathbf{r}) + \nu(\mathbf{r}), \tag{9}$$

where $\nu(\mathbf{r})$ is the noise term. In subsection 2.D, we briefly revisit how to estimate the modal coefficients of $B(\mathbf{r})$ from the discrete and noise-degraded $S(\mathbf{r})$ images. Before doing so, in subsection 2.C we outline the information that can be obtained from the Zernike coefficients themselves.

C. Significance of the Zernike Coefficients

Zernike polynomials are particularly well suited to describe typical all-sky night brightness distributions, in the sense that a truncated low-order expansion (with k ranging from 1 to a given maximum mode index M) usually provides a sufficiently close approximation to the actual values of $B(\mathbf{r})$. Once the corresponding M modal coefficients have been estimated, the information content of an all-sky image of several MB size can be compressed down to that set of M real numbers, usually with $M < 100$ in the case of cloudless and moonless images. Each Zernike coefficient describes the relative contribution of the associated mode to the overall night sky brightness pattern. Besides that, they provide some interesting additional information:

1. *Average and Zenithal Brightness*

The average sky brightness across the hemispherical FOV is directly given by the first Zernike coefficient, a_1, which corresponds to the piston term $Z_1 = 1$. This result is immediate from Eq. (8) for $k = 1$, taking into account that the all-sky images are equal-area projections.

The sky brightness at the zenith, $B(\mathbf{0})$, can be straightforwardly calculated in terms of the rotationally symmetric Zernike coefficients (in double-index notation, $a_{n,m}$ with n even and $m = 0$) as the weighted sum:

$$B(\mathbf{0}) = \sum_{n=0}^{\infty} (-1)^{\frac{n}{2}} \sqrt{(n+1)}\, a_{n,0}. \tag{10}$$

2. *Parseval's Theorem and Spatial Variance of the All-Sky Night Brightness Distribution*

From Eqs. (7) and (5), it follows that the Parseval's theorem in the Zernike space can be formulated as

$$\frac{1}{\pi} \int_{r=0}^{1} \int_{\theta=0}^{2\pi} |B(\mathbf{r})|^2 r \mathrm{d}r \mathrm{d}\theta = \sum_{k=1}^{\infty} a_k^2 \equiv \sum_{n=0}^{\infty} \sum_{m=-n}^{n} a_{n,m}^2. \tag{11}$$

This result allows us to compute the spatial average of the squared brightness distribution across the hemispheric FOV as the sum of the squares of the modal coefficients. Since a_1(i.e., $a_{0,0}$) is the average brightness itself, the spatial variance σ^2 of $B(\mathbf{r})$ is given by

$$\sigma^2 = \sum_{k=2}^{\infty} a_k^2 \equiv \sum_{n=1}^{\infty} \sum_{m=-n}^{n} a_{n,m}^2. \tag{12}$$

3. *Power Spectrum in the Zernike Space*

Given an ensemble of all-sky night brightness maps, its modal power spectrum in the Zernike space, $P(k)$, can defined as

$$P(k) = \langle a_k^2 \rangle \equiv \langle a_{n,m}^2 \rangle, \tag{13}$$

where $\langle\rangle$ denotes ensemble average. The $P(k)$ spectrum informs us about the expected power contribution of each individual mode to the overall sky brightness pattern at the observing site. In some cases, it is convenient to work with the radial power spectrum $P(n)$, which aggregates for each radial order n the ensemble-averaged power contributions of all its azimuthal modes:

$$P(n) = \sum_{m=-n}^{n} \langle a_{n,m}^2 \rangle. \tag{14}$$

D. Linear Fitting of All-Sky Night Brightness Maps

As stated above, the recorded all-sky maps $S(\mathbf{r})$ are discrete and noise-degraded versions of the actual night sky brightness distributions $B(\mathbf{r})$. Several methods can be used to estimate $B(\mathbf{r})$ from the available $S(\mathbf{r})$ data. The Zernike modal estimation approach consists in approximating $B(\mathbf{r})$ by a finite expansion $\hat{B}(\mathbf{r})$ up to a given mode M, such that

$$\hat{B}(\mathbf{r}) = \sum_{k=1}^{M} \hat{a}_k Z_k(\mathbf{r}), \tag{15}$$

and finding the set of estimated coefficients, $\hat{a}_k$, $k = 1, \ldots, M$, which best fit the recorded $S(\mathbf{r})$ according to some predefined merit criteria.

In absence of any *a priori* information about the statistical properties of the actual brightness coefficients, a_k, a sensible choice to determine the $\hat{a}_k$ is to perform a conventional linear least-squares fit providing the smallest Euclidean distance between the recorded and estimated images, evaluated at a suitable set of sampling points. To do so, first recall that the N pixels contained within the hemispherical FOV of the 2D all-sky image $S(\mathbf{r}_s)$, $s = 1, \ldots, N$, can be reordered as a column vector $\mathbf{s}$ of size $N \times 1$ whose elements are given by $s_s = S(\mathbf{r}_s)$. The noise affecting each pixel can be stacked in the same way as a $N \times 1$ vector $\boldsymbol{\nu}$ ($\nu_s = \nu(\mathbf{r}_s)$, $s = 1, \ldots, N$). On the other hand, arranging the unknown actual brightness coefficients as a column vector $\mathbf{a}$ of size $\infty \times 1$ such that $(\mathbf{a})_k = a_k$ and defining a Zernike matrix $\mathbf{Z}$ of size

$N \times \infty$ such that its elements are given by $(Z)_{sk} = Z_k(\mathbf{r}_s)$, Eqs. (7) and (9) can be combined and expressed in matrix form as

$$\mathbf{s} = \mathbf{Z}\mathbf{a} + \nu. \tag{16}$$

For the same set of sampling points, the brightness estimate in Eq. (15) can be rewritten as

$$\hat{\mathbf{b}} = \mathbf{Z}\hat{\mathbf{a}}, \tag{17}$$

where $\hat{\mathbf{b}}$ is a $N \times 1$ column vector whose elements are given by $\hat{b}_s = \hat{B}(\mathbf{r}_s)$, and $\hat{\mathbf{a}}$ is an $M \times 1$ vector containing the estimated coefficients $\hat{a}_k$ (whose values are to be determined). The simplest solution for $\hat{\mathbf{a}}$ can be sought as a set of linear combinations of the measurements weighted by the elements of a suitable reconstruction matrix $\mathbf{R}$, such that

$$\hat{\mathbf{a}} = \mathbf{R}\mathbf{s}. \tag{18}$$

The least-squares solution for $\mathbf{R}$ that minimizes the Euclidean distance $\|\mathbf{s} - \hat{\mathbf{b}}\|$ is given by the Moore–Penrose pseudoinverse [24,25]:

$$\mathbf{R} = (\mathbf{Z}_M^T \mathbf{Z}_M)^{-1} \mathbf{Z}_M^T, \tag{19}$$

where the superscript T stands for "transpose" and $\mathbf{Z}_M$ is a $N \times M$ matrix formed by the first M columns of $\mathbf{Z}$.

The Zernike decomposition of the all-sky night brightness maps hence proceeds as follows: once the highest mode M to be included in the $\hat{B}(\mathbf{r})$ expansion is chosen, the matrix $\mathbf{Z}_M$ is constructed by computing the values of the M Zernike polynomials at the $s = 1, \ldots, N$ sampling points. Note that these points may be either all the available points within the image or a subset of them of a convenient size. The only constraints in choosing them are that they have to be spatially distributed in a judicious way in order to perform an adequate spatial sampling of the sky brightness distribution and that they have to be enough in number as to avoid the potential ill-conditioning of the $\mathbf{Z}_M^T \mathbf{Z}_M$ matrix, which could prevent its successful numerical inversion. With $\mathbf{Z}_M$ at hand, the pseudoinverse $\mathbf{R} = (\mathbf{Z}_M^T \mathbf{Z}_M)^{-1} \mathbf{Z}_M^T$ can be easily computed and applied to the map data vector $\mathbf{s}$ to obtain the estimated coefficients $\hat{\mathbf{a}}$ according to Eq. (18), and subsequently the estimated all-sky night brightness distribution $\hat{B}(\mathbf{r})$ can be reconstructed using Eq. (15).

3. Results of the Measurement Campaign 2012–2013

The Zernike approach described in the previous section was applied to analyze the all-sky night brightness maps obtained with an All Sky Astronomical Monitor (AstMon) camera [16] at the Astronomical Observatory of Universidad Complutense de Madrid (40° 27′ 04″ N 03° 43′ 34″ W), located within Madrid City, during the period of November 2012 to November 2013.

In the AstMon camera, the full hemispheric sky (FOV 180 degrees) is imaged with a Sigma 4.5 mm F2.8 EX DC HSM Circular Fisheye lens onto a CCD QSI 583 ws whose detector is a Kodak KAF-8300 chip. The lens is designed to provide a zenithal equal-area (ZEA) projection. Images were taken through astronomical filters of 1.25 in. in diameter inserted in the optical path. All-sky images, in the B, V and R Johnson–Cousin's photometric bands [26], were continuously taken throughout each night. The effective wavelengths of these filters are 445, 551, and 658 nm, and the bandwidths (FWHM) 94, 88, and 138 nm for the B, V and R bands, respectively. After calibration [23,27], they were used to compute the corresponding night brightness maps as the one shown in Fig. 1.

Each map was stored as a FITS image of 2500 × 2500 pixels with the celestial vault mapped onto a circular region of radius 1150 pixels. A subset of the points within this circular region was used for the fit (one out of every 100, distributed in a square lattice). Points with altitude below 5.5° or clearly belonging to conspicuous artificial structures were excluded from this subset, since the aim was to fit the night sky brightness and not the artificial obstacles that may be present within the FOV (see the observatory domes and other artificial structures at the rim of Fig. 1). Typical fits involved about 36,000 data points. No denoising algorithms were used to preprocess the images before the fits.

We restricted our study to moonless and cloudless nights, focusing on the images taken at two different moments of the night, 21:30 and 02:00 UT, to study changes in the sky brightness due to the different use of public and private lighting. Maps were fitted using the first $M = 66$ Zernike modes (radial order $n_{\max} = 10$), since an expansion to that order (and even to lower ones) was found to be enough accurate to describe the measured all-sky maps with near noise-limited precision.

A. Individual All-Sky Maps

To illustrate the outcomes obtained when fitting individual maps, we report in this subsection the results corresponding to the ones taken at December 8, 2012, at 21:28 (UT), in the B, V (see Fig. 1), and R bands.

Figure 3 shows the values of the first 45 fitted coefficients for all three bands. The remaining ones (up to $M = 66$) have smaller magnitudes. The overall behavior in the three bands is similar, dominated by the contributions of the azimuthally symmetric modes ($a_{n,0}$ with n even, corresponding to $k = 1, 5, 13, 25\ldots$). As anticipated, these coefficients are positive, indicating a decrease of brightness from horizon to zenith. Their magnitude is generally higher in the R band than in the V and B (in that order) indicating correspondingly higher sky brightness levels. In particular, the brightness averaged across the FOV, given by the first Zernike coefficient,

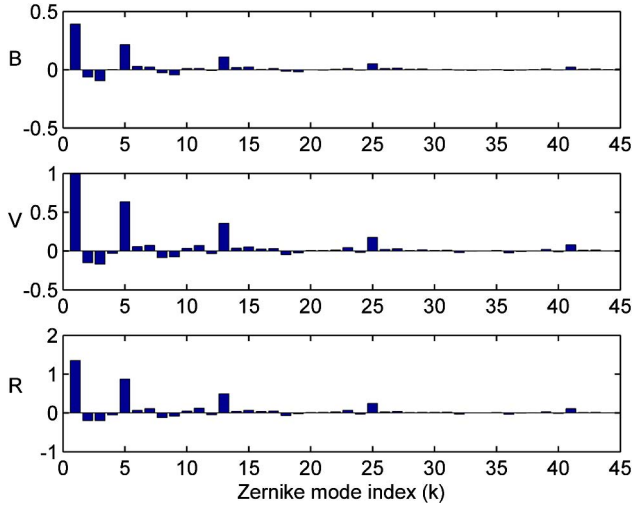

Fig. 3. Values of the first 45 estimated Zernike coefficients (in mJy/arcsec^2), corresponding to the all-sky night brightness maps taken at the astronomical observatory of Universidad Complutense, Madrid, on December 8, 2012, at 21:28 (UT), in the Johnson–Cousin's B, V (see Fig. 1), and R bands, plotted versus the Zernike mode index k.

is 1.35, 0.99, and 0.39 mJy/arcsec^2 for the B, V and R bands, respectively. Modes $a_{n,m}$ with n odd ($k = 2, 3, 7, 8, 9, 10\ldots$), and most notably the tilts ($a_{1,-1}$ and $a_{1,+1}$, $k = 2,\ 3$), have among others the overall effect of shifting the darkest point away from the zenith. They arise as a consequence of the uneven distribution of light sources around the observing site, reflecting the eccentric situation of the UCM campus with respect to Madrid city.

Figure 4 shows the original all-sky maps $S(\mathbf{r})$ (left column) and the reconstructed $\hat{B}(\mathbf{r})$ obtained using the 66 estimated modal coefficients for each band (right). Artificial obstacles at the horizon rim were excluded from the fits. These low-order reconstructed maps faithfully reproduce the brightness distribution of the original ones, avoiding pixel noise and point-like sky sources.

Figure 5 shows the profiles along the horizontal diameter of the original B-band map (thin black line) and the reconstructed one (thick red). The reconstructed profile strongly attenuates the effects of noise and is not affected by the presence of bright point-like celestial sources (Jupiter, in this example). The overall rms fit residuals average to 0.02, 0.04, and 0.05 mJy/arcsec^2 for the B, V and R bands, respectively, and for the most part correspond to the noise present in the original images, which is not reconstructed (nor attempted to) in the fitted ones.

B. Overall Results

Along the observation period 240 all-sky maps (one third in each band) fulfilled the selection criteria. The analysis of this ensemble provides some insights about the prevalent sky conditions on clear nights and its variability at the observing site.

Two relevant statistical descriptors of the night sky are the expected values of its Zernike coefficients,

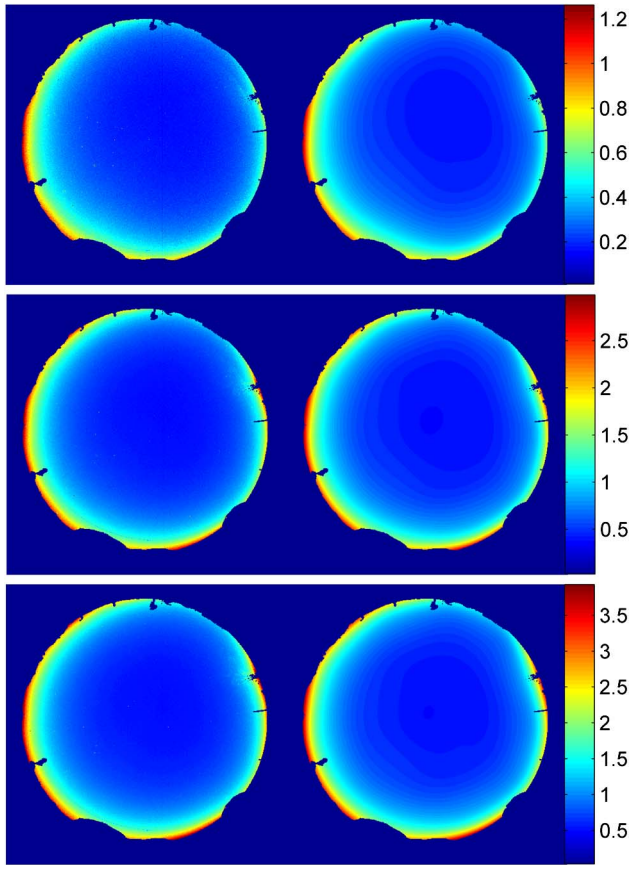

Fig. 4. Top to bottom: Color-coded versions of the original all-sky night brightness maps in the B, V and R bands (left) and reconstructed ones (right) with an expansion up to the Zernike radial order $n_{\max} = 10$ ($M = 66$ modes). The scale units are mJy/arsec^2. Note the different amplitude of the scale for each band.

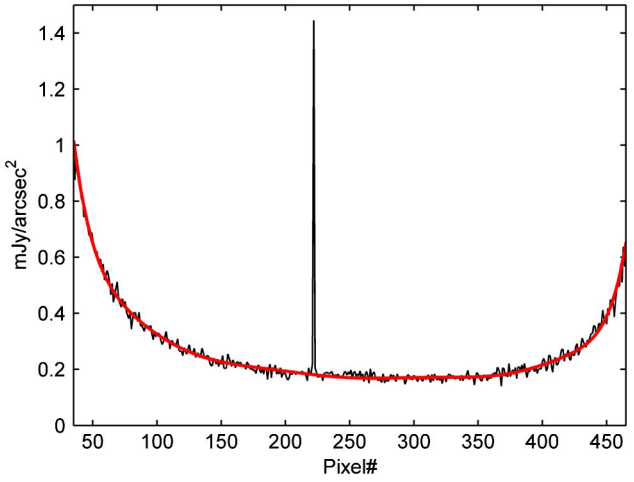

Fig. 5. Original (thin black line) and reconstructed (thick red line) profiles of the night sky brightness measured on the B-band image across an horizontal row, using sampled sky maps with resolution 500 × 500 pixels. Isolated point-like sources (Jupiter) do not show in the low-order Zernike fitting of the continuous sky brightness distribution.

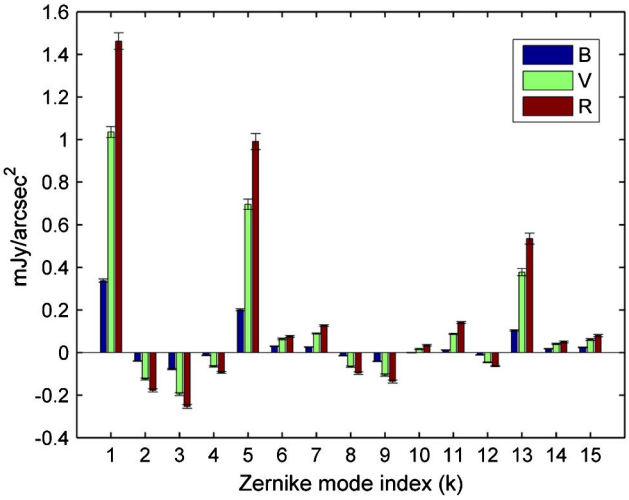

Fig. 6. Average values $\langle \hat{a}_k \rangle$ of the first 15 Zernike modes for the ensemble of cloudless and moonless nights (see text) in the B, V and R bands. Error bars correspond to one standard deviation of the mean (80 images for each band).

$\langle \hat{a}_k \rangle$, and its Zernike power spectrum. In the bar diagram of Fig. 6, we show the average values of the first 15 Zernike coefficients (up to $n = 4$) and the standard deviation of their mean (80 data points for each band). The remaining coefficients up to $M = 66$, not shown here to avoid cluttering the graph, follow a similar trend. Most coefficients are significantly different from zero, the main contributions arising from azimuthally symmetric modes, with positive sign. Tilts ($k = 2, 3$) and comatic terms ($k = 7$, 8, 9, 10) also contribute significantly to the overall pattern, as do low-order n even modes with m-fold symmetry (like the astigmatic $k = 4$, 6, and tetrafoil $k = 11$, 15, terms). The variability, measured by the standard deviation of the mean, is relatively small for all modes.

Figure 7 displays the modal and radial Zernike power spectra $P(k)$ and $P(n)$ given by Eqs. (13) and (14), respectively, computed using the estimated coefficients of the 80 maps in each band. Both show an overall monotonic decreasing trend. Particularly interesting is the behavior of the radial power spectra $P(n)$ shown in the lower plot. The magnitude of the contributions of the n-even orders and the n-odd ones decreases at about the same pace within each band, but from different initial values depending on the order parity. Even radial orders are composed of modes having azimuthal or even-fold rotational symmetry, whose gradient averaged over the hemispherical field is zero. Odd radial orders, in turn, correspond to general comatic terms (including tilts) that indicate the presence of overall brightness gradients and hence carry information about the location of the observing site relative to the light sources. As a rule of thumb, the contribution of the n-odd orders tends to be about one order of magnitude smaller than that of their preceding even ones. The $P(n)$ dependence is approximately linear in a logarithmic scale, with a slope close to −2.5 dB per

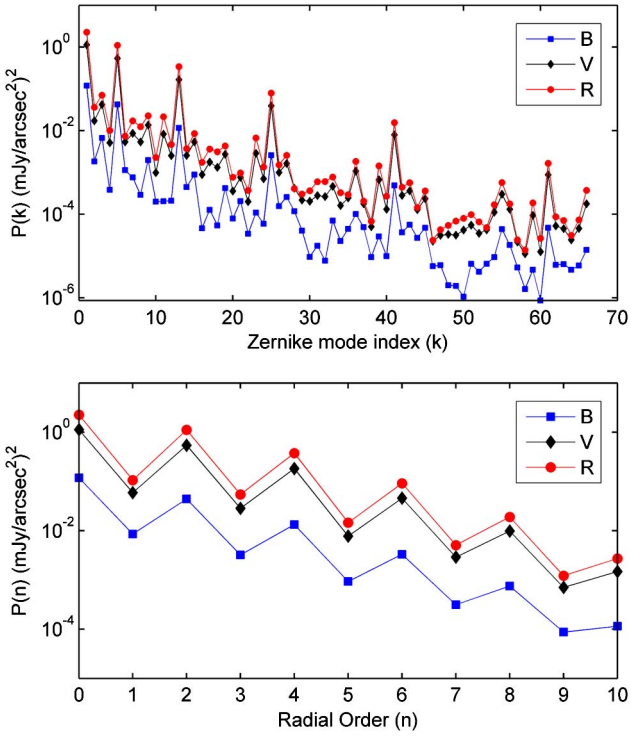

Fig. 7. Top: $P(k)$, power spectrum in the Zernike space of the ensemble of all-sky maps analyzed in this work (B, V and R bands). Bottom: Spectral power distribution aggregated by whole radial orders, $P(n)$.

radial order. The $P(n)$ power spectrum informs us about the expected relative weight of each complete radial order in the composition of the all-sky brightness patterns and, under the assumption that it can be cautiously extrapolated to higher n values, provides useful guidelines to choose the maximum radial order $n_{\max}$ (or mode index M) up to which expand the estimated brightness defined in Eq. (15).

An interesting issue is related to the changes experienced by the sky brightness levels at different hours of the night. It is expected that the overall brightness of urban skies should decrease as residential, commercial, vehicle, and ornamental lighting is progressively switched off when people ends its active daily period, a trend that has been reported at several locations using low-spatial-resolution photometric devices [28–32].

To study this dependence using all-sky maps, we computed both the sky brightness at the zenith [Eq. (10)] and its spatial average across the FOV, a_1, for the complete subsets of images taken at 21:30 and 02:00 UT during the observation period. Their means and uncertainties are listed in the first two data columns of Table 1.

A more meaningful assessment of these changes can be obtained from the analysis of the brightness ratios 02:00/21:30 corresponding to each individual night. To compute them, we selected the subset of nights having appropriate images at both moments of the night, getting a total of 18 image pairs (not all pairs of the original sample fulfilled that

Table 1. Average and Zenithal Brightness

	Average brightness across the FOV (mJy/arcsec^2)		
Band	21:30 UT[a]	02:00 UT[a]	Ratio[b]
B	0.396 [0.006]	0.280 [0.005]	0.70 [0.01]
V	1.12 [0.03]	0.95 [0.04]	0.84 [0.02]
R	1.54 [0.05]	1.38 [0.06]	0.89 [0.03]
	Zenithal brightness (mJy/arcsec^2)		
Band	21:30 UT[a]	02:00 UT[a]	Ratio[b]
B	0.162 [0.002]	0.110 [0.001]	0.672 [0.010]
V	0.391 [0.006]	0.320 [0.005]	0.808 [0.008]
R	0.528 [0.010]	0.460 [0.008]	0.860 [0.012]

[a]Mean value [standard deviation of the mean] of the brightness, computed using the whole subsets of images taken at 21:30 UT or 02:00 UT.

[b]Mean value [standard deviation of the mean] of the brightness ratio 02:00/21:30, computed using the 18 image pairs belonging to the same nights.

requirement, mainly due to the presence of the Moon at the first or second half of the night). The mean and the uncertainty of these brightness ratios are listed in the last column of Table 1.

Unlike previous studies, these data correspond to standard BVR photometric bands. The average and zenithal brightness levels are consistently higher at both moments for band R followed by V and B in agreement with what can be expected from Figs. 6 and 7. In all cases the average brightness is about 2.5 to 3 times higher than the associated zenithal brightness.

Between the first and second halves of the night, the brightness levels in the B band, both averaged and zenithal, suffer a significantly more pronounced decrease than those of the V and R bands, as shown in the last column of the table. In the context of our present measurements this behavior can be likely attributed to the switch-off of the ornamental lighting (mostly based on metal-halide lamps with strong emission in the B-band) around midnight, whereas the street lamps (mostly high-pressure sodium) are kept on throughout the whole night. Using the method described above one can easily obtain that the sky color of Madrid is bluer during the first part of the night. This result confirms previously reported measurements made using low spatial resolution devices [29,33].

4. Additional Remarks

In this work, we have purposely dealt with cloudless and moonless night sky maps. Preliminary results not included here show that the Zernike decomposition approach can also be successfully applied to analyze total or partially clouded skies at the expense of increasing the radial order of the fit, and hence the number of coefficients, to account for the more irregular brightness distributions produced by broken clouds. The effects of clouds on the night sky brightness at the red, green, and blue bands have been thoroughly analyzed by Kyba *et al.* [31] using low-spatial-resolution detectors. The research of the color changes in the photometric B, V and R bands under cloudy skies using all-sky maps and Zernike modes is presently under way.

The all-sky maps analyzed in this paper displayed spectral radiances. The same Zernike decomposition approach can be used to fit maps of the total radiance within each photometric band, expressed in Watts/($m^2 \cdot sr$), or brightness given in the widely used logarithmic scale of magnitudes per square arcsecond (mag/arcsec^2). Radiance maps in SI units offer the possibility of taking full advantage of additivity: the Zernike coefficients of any all-sky map expressed in radiance units are equal to the sum of the coefficients of the individual all-sky maps that would be produced separately by each of the light sources contributing to it. This useful property is lost when mag/arcsec^2 units are used instead.

Modal expansions of this kind allow to compress in an efficient way the all-sky map information, give analytical expressions for the night sky brightness, provide modal coefficients with definite physical meaning and help filtering the noise. A characteristic feature of modal expansions is that the brightness at any point of the sky is expressed as the sum of the contributions of a set of individual modes (in our case, the Zernike polynomials), which are defined over the whole surface of the all-sky map. The modal coefficients are computed as linear combinations of all available measurements. In turn, zonal approaches like the ones based on spline surface models [15] compute the brightness at any given direction mostly as a function of the values it takes at the neighboring measurement points.

Whether is it better to use zonal or modal approaches is an issue largely dependent on the problem to be handled. For relatively smooth distributions like those corresponding to the scattering of light in the atmosphere, modal approaches tend to require a substantially smaller number of parameters (the Zernike coefficients) than their zonal counterparts. Besides, the geometrical shape of the Zernike modes seems particularly well suited to describe typical night sky brightness patterns. Whereas the low-order modes provide the basis for

fitting the slowly variant spatial structure of the light polluted sky, high-order modes (that only take appreciable values near the unit circle rim) are instrumental to fit the relatively high brightness gradients present near the horizon due to the artificial light sources. In the examples here analyzed, low order expansions up to $n_{\max} = 10$ (corresponding to the first 66 Zernike terms) were enough to capture the relevant features of all-sky maps taken in the B, V and R Johnson's astronomical photometric bands. Additionally, modal Zernike expansions provide an analytical and grid-independent description of the all-sky brightness that may facilitate the intercomparison of results with those obtained at other observing sites using different instruments and/or measurement grids.

Zernike fits are also instrumental to filter out image noise and the direct radiance contributions arising from isolated point-like sources of natural or artificial origin. Noise reduction is achieved by choosing the number of modes included in the expansion, M, in such a way that the smooth sky brightness distribution be correctly reproduced by the truncated series but the high spatial frequency fluctuations of the image brightness due to random noise in neighboring pixels and isolated sources of small size be removed, appearing as residuals of the fit. This noise reduction approach, that can be termed as modal, is different from but compatible with zonal strategies that address noise reduction at a local level, such as the one successfully applied by Duriscoe *et al.* [15], who determine the brightness of the sky background by dividing the entire sky into small regions of about 1 deg in diameter and taking in each one the median of the pixel values. Note that both strategies could be combined and used together, e.g., by performing a zonal noise reduction before proceeding to the Zernike fit.

The attenuation of the high spatial frequencies obtained with truncated Zernike fits can alternatively be described as a low-pass filtering operation in the Zernike space. Note that Eqs. (7) and (8) define what can be termed a Zernike transform pair, by virtue of which any real function defined on the unit-radius circle is transformed into another real function $a(k) = a_k$ $(k = 1, \ldots, \infty)$, which constitutes its Zernike spectrum. Approximating the original function by a truncated Zernike expansion, instead of using the formally infinite series required to represent it exactly, is equivalent to performing a low-pass filtering of its spectrum. These considerations are meant to be applied to the measured sky brightness $S(\mathbf{r})$ given by Eq. (9), which is composed of a relatively low spatial frequency signal $B(\mathbf{r})$, and the noise $\nu(\mathbf{r})$ whose Zernike spectrum attains appreciable values up to very high values of k.

As such, the Zernike expansions here described can be used without any essential modification to analyze the all-sky night brightness maps obtained using other techniques, e.g., those obtained by Duriscoe *et al.* [15] from calibrated images of the night sky taken with wide-field CCD cameras. In an analogous way, they could be applied to analyze the numerical all-sky night brightness distributions predicted by different theoretical models [7–12].

An interesting possibility, not dealt with in this paper, stems from the fact that the cloudless and moonless light-polluted skies can be satisfactorily described by finite sets of Zernike coefficients of relatively small size. This result, together with the knowledge of the general shape of the Zernike power spectrum, opens the way for developing optimum estimation algorithms [25] that should allow us to retrieve the continuous all-sky night brightness distribution from a small set of narrow-field measurements made in different directions appropriately distributed throughout the sky. The same principle could be useful for reducing the computational load of the all-sky maps calculated from theoretical models, by expressing the continuous brightness distributions as truncated series of Zernike polynomials and estimating their modal coefficients from the brightness predicted at a discrete set of points of reasonably small size. Further work is required to assess the possibilities and limitations of this approach.

5. Conclusions

All-sky night brightness maps can be successfully described and analyzed in terms of Zernike polynomials. The Zernike coefficients of each map can be easily estimated by a conventional linear least-squares fit. Low-order expansions up to $n_{\max} = 10$, corresponding to the first 66 Zernike terms, seem to be enough to capture the relevant features of all-sky maps taken in cloudless and moonless nights, in the B, V and R Johnson–Cousin's photometric bands.

Besides the clear benefits of compressing the relevant image information into a small-sized coefficients vector, providing an analytical expression for the night sky brightness, and alleviating the effects of noise, the Zernike expansions allow us to quantify in a straightforward way the average and zenithal sky brightness, and its variation across the FOV, providing an easy framework to analyze the evolution of these magnitudes throughout the night and in the long term.

Our results, based on the all-sky images taken at the UCM Astronomical Observatory during the campaign 2012–2013, show that the Zernike composition of the Madrid night skies at that site is mainly determined by the azimuthally symmetric modes, with strong contributions from coma-like terms (including tilts) that reflect the eccentric situation of the observing place relative to the city lights. The Zernike power spectrum of the sky in the B, V and R bands tends to decrease monotonically with the radial order n, with an overall slope of about –2.5 dB per order. The contribution of the even and odd radial orders decreases nearly at the same rate with n, but starting from different initial values.

We have found that both the zenithal sky brightness as well as the brigthness averaged across the hemispherical FOV are higher at the R band, followed by the V and B at both halves of the night. Between the first and second half of the night, the decrease of brightness in the B band, both averaged and zenithal, is significantly more pronounced than those of the V and R bands.

Although the observational data presented in this work refer to a particular urban site, its overall conditions, not untypical of those prevailing at densely populated cities, suggest that the general results reported here about the Zernike composition of all-sky night brightness maps may be representative of cloudless and moonless skies at this kind of locations.

This work was partially funded by the Xunta de Galicia, Programa de Consolidación e Estruturación de Unidades de Investigación Competitivas, grant CN 2012/156, the Spanish Ministry of Science and Innovation MICINN (AYA2012-30717, AYA2012-31277, and FPA2010-22056-C06-06), the Spanish program of International Campus of Excellence Moncloa (CEI) and the Madrid Regional Government through the AstroMadrid Project (CAM S2009/ESP-1496). A. Sánchez de Miguel was supported by an FPU grant from MICINN. This work was developed within the framework of the Spanish Network for Light Pollution Studies (Ministerio de Economía y Competitividad, Acción Complementaria AYA2011-15808-E) whose support is also acknowledged.

References

1. P. Cinzano, F. Falchi, and C. Elvidge, "The first world atlas of the artificial night sky brightness," Mon. Not. R. Astron. Soc. **328**, 689–707 (2001).
2. M. F. Walker, "The California site survey," Publ. Astron. Soc. Pac. **82**, 672–698 (1970).
3. F. Hölker, C. Wolter, E. K. Perkin, and K. Tockner, "Light pollution as a biodiversity threat," Trends Ecol. Evol. **25**, 681–682 (2010).
4. K. Thapan, J. Arendt, and D. J. Skene, "An action spectrum for melatonin suppression: evidence for a novel non-rod, non-cone photoreceptor system in humans," J. Physiol. **535**, 261–267 (2001).
5. D. M. Berson, F. A. Dunn, and M. Takao, "Phototransduction by retinal ganglion cells that set the circadian clock," Science **295**, 1070–1073 (2002).
6. M. S. Rea, M. G. Figueiro, A. Bierman, and R. Hamner, "Modeling the spectral sensitivity of the human circadian system," Lighting Res. Technol. **44**, 386–396 (2012).
7. M. Kocifaj, "Light-pollution model for cloudy and cloudless night skies with ground-based light sources," Appl. Opt. **46**, 3013–3022 (2007).
8. M. Kocifaj, "Light pollution simulations for planar ground-based light sources," Appl. Opt. **47**, 792–798 (2008).
9. P. Cinzano and F. Falchi, "The propagation of light pollution in the atmosphere," Mon. Not. R. Astron. Soc. **427**, 3337–3357 (2012).
10. R. H. Garstang, "Model for artificial night-sky illumination," Publ. Astron. Soc. Pac. **98**, 364–375 (1986).
11. M. Kocifaj, "A numerical experiment on light pollution from distant sources," Mon. Not. R. Astron. Soc. **415**, 3609–3615 (2011).
12. M. Aube and M. Kocifaj, "Using two light-pollution models to investigate artificial sky radiances at Canary Islands observatories," Mon. Not. R. Astron. Soc. **422**, 819–830 (2012).
13. K. Tohsing, M. Schrempf, S. Riechelmann, H. Schilke, and G. Seckmeyer, "Measuring high-resolution sky luminance distributions with a CCD camera," Appl. Opt. **52**, 1564–1573 (2013).
14. O. Rabaza, D. Galadí-Enríquez, A. Espín-Estrella, and F. Aznar-Dols, "All-sky brightness monitoring of light pollution with astronomical methods," J. Environ. Manage. **91**, 1278–1287 (2010).
15. D. M. Duriscoe, C. B. Luginbuhl, and C. A. Moore, "Measuring night-sky brightness with a wide-field CCD camera," Publ. Astron. Soc. Pac. **119**, 192–213 (2007).
16. J. Aceituno, S. F. Sánchez, F. J. Aceituno, D. Galadí-Enríquez, J. J. Negro, R. C. Soriguer, and G. Sanchez-Gomez, "An all-sky transmission monitor: ASTMON," Publ. Astron. Soc. Pac. **123**, 1076–1086 (2011).
17. F. Zernike, "Beugungstheorie des Schneidenverfahrens und seiner verbesserten Form, der Phasenkontrastmethode," Physica **1**, 689–704 (1934).
18. M. Born and E. Wolf, *Principles of Optics* (Cambridge University, 1998), pp. 464–466, 767–772.
19. V. Lakshminarayanan and A. Flecka, "Zernike polynomials: a guide," J. Mod. Opt. **58**, 545–561 (2011).
20. American National Standards Institute, Methods for Reporting Optical Aberrations of Eyes, Z80.28-2004 (ANSI, 2004).
21. L. N. Thibos, R. A. Applegate, J. T. Schwiegerling, and R. Webb, and VSIA Standards Taskforce Members, "Standards for reporting the optical aberrations of eyes," in *Vision Science and Its Applications 2000*, V. Lakshminarayanan, ed., OSA Trends in Optics and Photonics Series (Optical Society of America, 2000), Vol. **35**, pp. 232–244.
22. M. R. Calabretta and E. W. Greisen, "Representation of celestial coordinates in FITS," Astronomy and Astrophysics **395**, 1077–1122 (2002).
23. M. Nievas Rosillo, "Absolute photometry and night sky brightness with all-sky cameras," Master's thesis, (Universidad Complutense de Madrid, 2013), http://eprints.ucm.es/24626/.
24. J. Herrmann, "Least-squares wave front errors of minimum norm," J. Opt. Soc. Am. **70**, 28–35 (1980).
25. P. B. Liebelt, *An Introduction to Optimal Estimation* (Addison-Wesley, 1967).
26. M. S. Bessell, "UBVRI photometry II: the Cousings VRI syatem, its temperature and absolute flux calibration, and relevance for two-dimensional photometry," Publ. Astron. Soc. Pac. **91**, 589–607 (1979).
27. M. Nievas Rosillo, "*Fotometría absoluta y brillo de fondo de cielo con AstMon-UCM*," (Universidad Complutense de Madrid, 2012), http://eprints.ucm.es/16974/
28. S. Darula, "Windows in buildings: potential source of light pollution," in *Proceedings of the International Conference on Light Pollution Theory, Modelling and Measurements*, Smolenice, Slovak Republic (2013) pp. 51–56.
29. A. Sánchez de Miguel, "*Variación del brillo del fondo de cielo en el cénit con la fase y altura de la Luna*," (Universidad Complutense de Madrid, 2013), http://guaix.fis.ucm.es/~alex/TFG_Alex_v3.pdf.
30. J. Puschnig, T. Posch, and S. Uttenthaler, "Night sky photometry and spectroscopy performed at the Vienna University Observatory," J. Quant. Spectrosc. Radiat. Transfer (2013). Available online 4 September 2013.
31. C. C. M. Kyba, T. Ruhtz, J. Fischer, and F. Hölker, "Red is the new black: how the colour of urban skyglow varies with cloud cover," Mon. Not. R. Astron. Soc. **425**, 701–708 (2012).
32. C. S. J. Pun and C. W. So, "Night-sky brightness monitoring in Hong Kong. A city-wide light pollution assessment," Environ. Monit. Assess. **184**, 2537–2557 (2012).
33. J. Zamorano, A. Sánchez de Miguel, J. Gómez Castaño, F. Ocaña, J. Gallego, B. Pila Díez, M. Nievas, C. Tapia, A. Fernández, and S. Pascual, "Night sky brightness and light pollution in Comunidad de Madrid," in *International Conference on Light Pollution Theory, Modelling, and Measurements*, Smolenice, Slovak Republic, 15-18 April 2013, http://eprints.ucm.es/24201/).